PCCP

ROYAL SOCIETY OF CHEMISTRY

PAPER

View Article Online
View Journal | View Issue

Cite this: *Phys. Chem. Chem. Phys.*, 2026, **28**, 3109

Strategy for steganography and information encryption–decryption using Fs laser-created luminescence in organic solids

Ruyue Que, [a] Olivier Plantevin, [b] Matthieu Lancry [a] and Bertrand Poumellec *[a]

Received 12th June 2025,
Accepted 8th January 2026

DOI: 10.1039/d5cp02244d

rsc.li/pccp

Functional materials, especially luminescent ones, are attracting increasing attention in the field of information security due to their potential in advanced steganography, information encryption–decryption, and anti-counterfeiting (IEDAC) technologies. However, current luminescence based IEDAC methods face several challenges, including risks of information leakage, ease of duplication, and sensitivity to environmental conditions, which limit their practical application. In this work, we demonstrate an IEDAC approach utilizing photoluminescence (PL) emission patterns generated by infrared femtosecond (fs) laser direct writing with their properties further tailored *via* post-exposure to linearly polarized continuous-wave (CW) laser. This method enables hierarchical two-level information storage: level-1 information is inscribed by creating PL in an organic substrate using fs laser direct writing, while level-2 information is concealed and encrypted through polarization-dependent excitation anisotropy in PL, which arises from polarization-selective bleaching of asymmetric luminophores induced by linearly polarized CW laser exposure. This technique not only allows polarization-based encoding, but also enhances security against brute-force attacks and reduces susceptibility to the environment. Validated across three different organic materials, with detailed results presented for Zeonex polymer, this method not only demonstrates its effectiveness but also suggests a versatile and universal approach for advancing IEDAC technology in the field of information security.

1. Introduction

In the era of digital proliferation, the importance of information security cannot be overstated. Information encryption–decryption and anti-counterfeiting (IEDAC) technology plays a vital role in protecting sensitive information in fields such as finance, healthcare, and government, preventing data breaches, theft, and other cyber threats.[1–3] Ongoing research efforts are focused on developing innovative and efficient IEDAC technologies, with particular emphasis on advanced functional materials.[4–6] Typically, designing functional materials for IEDAC involves three major steps: (1) material selection, (2) fabrication of functional structures, and (3) integration of an encryption algorithm.

Material selection is driven by specific optical properties suitable for secure information handling. Among these, luminescent materials stand out for their visual identifiability, multicolour emissions, high throughput, and design simplicity.[7–9] A wide variety of luminescent systems have been explored, including perovskite nanocrystals,[9] rare-earth nanoparticles,[10–12] plasmonic materials,[13] quantum dots (QDs)[14] and various polymer matrices.[15] These platforms support multiple luminescence modes such as photoluminescence,[7,9,16] phosphorescence,[3,4] mechano-luminescence,[2] and long-persistent luminescence,[17,18] offering versatile tools for IEDAC applications.

Research in this field has focused on enhancing luminescence through doping,[10,19] surface modification,[6,20,21] self-assembly,[22] and host-matrix incorporation.[7] For example, doping allows precise control over dye concentration and distribution to produce specific optical properties in the material with uniform colour, while this method can be time-consuming and lack spatial selectivity. Surface modification *via* lithography or deposition can achieved nano-level resolution but is typically limited to 2D surfaces. Moreover, methods like pre-designed masks[23] and inkjet printing[24] often leave writing traces, potentially exposing the encryption pattern to adversaries.[17]

There are also practical challenges to the application of IEDAC in different scenarios. For example, the photoemission efficiency and stability in some optical functional materials may diminish in the aggregated state.[25] Simple optical

[a] *Université Paris-Saclay, CNRS, Institut de chimie moléculaire et des matériaux d'Orsay, SP2M, 91405, Orsay, France. E-mail: bertrand.poumellec@universite-paris-saclay.fr*
[b] *Université Paris-Saclay, CNRS, Laboratoire de Physique des Solides, 91405, Orsay, France*

encryption materials with single-color static photoluminescence (PL) patterns are easily duplicated using materials with similar static PL properties,[26] underscoring the need for multicolour and multimode PL patterns to enhance security.[11] Another critical issue is the susceptibility to environmental factors such as temperature, humidity, and pH changes, which can lead to instability and data degradation.[27]

In addition to material development, the final step in IEDAC design involves integrating encryption algorithms. Typically, this process employs laser engraving, holography, or the use of diffractive optical elements to create text, images, or patterns on various materials.[28,29] These materials usually possess unique properties, such as temperature dependence, incident angular dependence,[6,20] excitation wavelength dependence,[10] upconversion,[11,30] photochromic,[31] dynamic PL,[16] circular dichroism,[29] polarization dependence,[32] among others. Particularly, a key feature is polarization dependence, which allows information retrieval only under correct polarization states. For example, nonlinear multilayer metamaterial holograms exhibit distinct third-harmonic images under orthogonal polarizations,[33] and certain nanostructures respond selectively to left- or right-circularly polarized light enabling design of anti-counterfeiting[34] and multidimensional information encryption.[12]

Therefore, to enhance information security, researchers are continuously developing advanced encryption materials by exploring a broad range of material types, fabrication techniques, and algorithmic strategies. Beyond these core attributes, effective encryption materials must also meet additional requirements: including fast writing ability, large data storage capacity, stability, reusability or erasability, compatibility of materials, low energy consumption *etc.*[35] Meeting all these criteria simultaneously remains a significant challenge.

Ultrafast laser has emerged as a powerful tool in this context due to its inherent advantages, such as a simple step, high peak power, spatial selectivity (3D), and fine resolution. Ultrafast laser-induced modifications in inorganic materials have already been successfully implemented for high-density 3D data storage.[36] Moreover, the development of functional nanostructures—such as nanogratings[37] and nanocrystals[38]—has further advanced the realization of multidimensional information storage system.[39] In the meantime, comparable resolutions can be achieved in organic materials,[40] which additionally offer functionalities like PL, expanding the dimensions and channels of information.[41–43] Importantly, whether the medium is organic or inorganic, the laser-embedded functional regions are typically robust, stable, and resistant to environmental degradation.[44]

Building on these advantages, recent advancements have further pushed the boundaries of fs-laser structuring towards the field of information security, ranging from biomimetic multi-band encryption[45] to metasurface-based structural coloration.[46] However, distinct from these structural modulations, the development of rewritable and concealed information storage based on molecular-level mechanisms in organic solids remains a significant frontier to be explored.

In this work, we present a strategy to locally store, conceal and encrypt information in 3D within organic solid substrate. This method leverages fs laser direct writing (FLDW) to inscribe permanent modifications that exhibit PL—serving as Level-1 information. A subsequent exposure to linearly polarized CW laser light (the post-exposure step) enables the generation and control of excitation polarization anisotropy in the PL signal, creating an additional layer of concealed information (level-2). This level-2 information remains invisible without the correct probing polarization orientation, effectively serving as a decryption key. Both encryption and decryption process can be performed using standard optical setups equipped with polarization control, making the method accessible and practical. Furthermore, this anisotropy orientation is shown to be rewritable and applicable to various materials, with detailed demonstrations in Zeonex polymer included in the main text. This approach not only expands the functional capacity of PL-active organic materials but also offers a versatile and secure platform for steganography, encryption, and anti-counterfeiting applications.

2. Results

2.1. Luminescence creation by IR fs laser

Infrared (IR) femtosecond (fs) laser direct writing (FLDW) was employed to locally induce permanent modifications with photoluminescence (PL) properties in a cyclic olefin polymer (Zeonex R790), as displayed in Fig. 1(a) and (b). This kind of polymer is of high interest due to its promising optical properties,[47] including transparency across a wide spectrum from UV to IR. The experimental procedure for the FLDW process follows the methods described in the previous work.[42] The laser-induced PL includes multiple excitation centers ranging from UV to green and emits light from blue to orange accordingly.[42] In this work, we focus on a specific species that is excitable at 448 nm as highlighted in the excitation spectra shown in Fig. 1(c). Fig. 1(c) also illustrates the emission spectrum excited by 448 nm has a peak at 510 nm and the emission spectrum excited by 468 nm is peaking at 520 nm. Accordingly, the 510 nm emission under 448 nm excitation is selected for analyzing excitation anisotropy. Using appropriate laser parameters, fs laser writing can encode information into the transparent polymer up to a few microns resolution,[42]

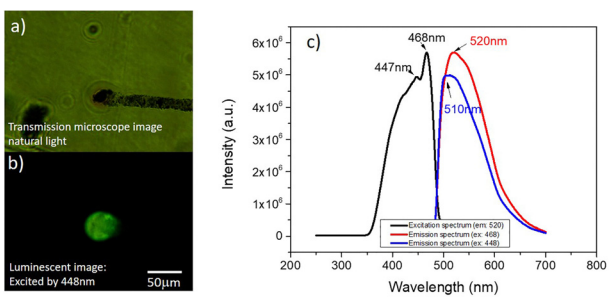

Fig. 1 (a) Transmission optical image of an irradiated line under natural light (the background color is due to the filter). fs laser parameters: repetition rate (RR) = 1 MHz, E_p = 30 nJ, scanning speed = 10 μm s^{-1}, polarization = 150°. (b) Luminescent image of the same line in (a), excited by 448 nm. (c) Excitation spectrum (black curve) of emission at 520 nm; emission spectra under 447 nm excitation (blue curve) and 468 nm excitation (red curve).

comparable to the studies in PDMS and PMMA substrates.[41,48] This encoded information, referred to as level-1 information, can be read out through a conventional optical microscope as black-white pattern under natural light and luminescent features under suitable excitation light.

2.2. Excitation anisotropy creation for encryption and decryption

Beyond the photoluminescence (PL) generated by fs-laser writing in this polymer, we further identified a polarization-sensitive excitation behavior. This property enables the introduction—or encryption—of angular excitation anisotropy, where the emission intensity becomes modulated according to the orientation of the linearly polarized excitation light. The angular position of maximum modulation depends on the polarization direction used during encryption. This polarization-dependent PL behavior serves as the basis for level-2 information, which can be both written and read using the optical setup illustrated in Fig. 2. In this setup, a 448 nm CW laser (with a 10 nm bandwidth) serves as the excitation source for both encryption and decryption processes. The laser spectrum is shown in the top-right corner of Fig. 2. The excitation light is linearly polarized, with its polarization orientation controlled *via* a control unit (highlighted by the orange dashed box in Fig. 2), which consists of a linear polarizer and a half-wave plate. A polarization angle of 0° (±2°) is defined with respect to the *x*-axis of the system platform. A dichroic mirror (Thorlabs, DMLP490R) is used to reflect excitation laser light to the sample and block it from the spectrometer. The CW laser power arriving on the sample was measured to be around 1.78 mW cm^{-2} during encryption and 0.44 mW cm^{-2} during decryption. Emission above 490 nm is collected either by a camera positioned above the microscope or by a spectrometer. To further suppress residual excitation light, a long-pass filter with a cutoff wavelength of 455 nm is placed in the detection path. Note that the luminescence intensity at 510 nm, excited by light with various polarization angles, was recorded using a spectrometer without emission polarization selection. The probing (*i.e.*, excitation) duration for each polarization angle step was approximately 1 second. Spectra acquisition was performed with a step size of 1 nm and a spectral resolution of 15 nm.

Since the optical setup incorporates multiple polarization-sensitive components—including a half-wave plate, dichroic mirror, focusing lens, and metallic mirror—the system's intrinsic anisotropy was analyzed and calibrated. Details of this calibration procedure are provided in SI S1. Additionally, irreversible bleaching was observed during measurements, as also detailed in SI S1.

After fs laser irradiation, the induced PL initially exhibits no dependence on the excitation polarization. This is shown by the black curve in Fig. 3(c), which has been corrected for both system anisotropy and bleaching effects. The absence of polarization dependence indicates that the initial PL is isotropic with respect to excitation polarization. However, this isotropy can be broken through post-exposure using linearly polarized CW light at 448 nm. We applied a 2-minute post-exposure to area 1 with a polarization angle of 0°, while same exposure at 90° to area 2, as illustrated in Fig. 3(a) and (b). The resulting excitation-dependent emission, shown by the blue and red fitting curves in Fig. 3(c), demonstrates a distinct anisotropic behavior: the emission intensity reaches a minimum when the probing (excitation) polarization is aligned with the post-exposure direction, and a maximum when it is perpendicular.

This directional dependence of emission on excitation polarization is referred to as excitation anisotropy. Additional polarization angles were tested and are presented in SI S2. Therefore, while the fs laser-induced PL is inherently isotropic, the subsequent exposure to linearly polarized CW light introduces excitation anisotropy, enabling the concealment of additional directional information. This embedded information is closely linked to the polarization direction used during post-exposure, offering a mechanism for secure data encoding.

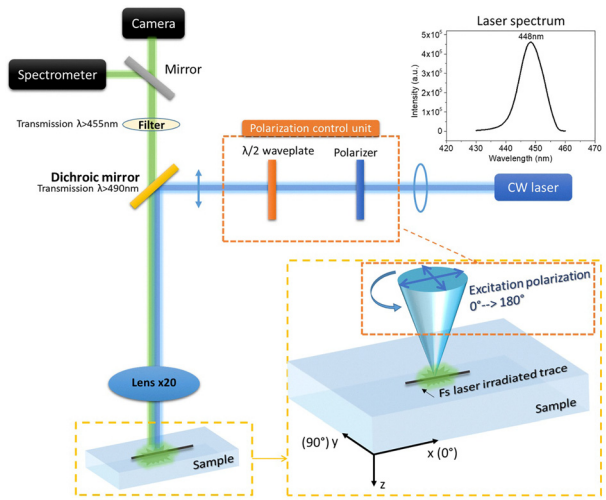

Fig. 2 Schematic diagram of the encryption–decryption setup; the orange dashed box displays the polarization control unit which consists of a polarizer and a half-wave plate, allowing the excitation light to be linearly polarized and oriented at any angle in the horizontal plane. The yellow dashed box displays a zoom of the sample, showing the axes reference of polarization direction that used in this paper; CW 448 nm laser spectrum is shown from 430 nm to 460 nm.

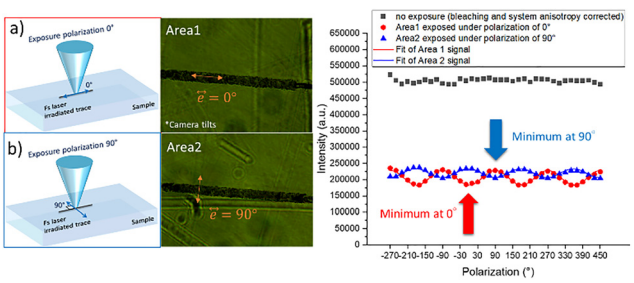

Fig. 3 (a) and (b) Schematic of post-exposure procedure with linearly polarized CW light at 0° and 90° applied to 2 sample areas; (c) PL intensity at 510 nm under 448 nm excitation, probed by excitation polarization from −270° to 450°. The black dots correspond to intensity of the area without post-exposure; the red and blue dots and fitting curves correspond to areas post-exposed at 0° and 90°, respectively. Fitting parameters can be found in SI S1. The fs laser irradiation conditions: E_p = 50 nJ, RR = 1 MHz, scanning speed:10 μm s^{-1}.

2.3. Re-orientation of the excitation anisotropy

Fig. 4 presents the excitation polarization–dependent photoluminescence intensity of a fixed area 3 subjected to alternating post-exposures with linear polarization at 0° and 90°, each lasting 300 s. All curves have been corrected for system-induced anisotropy (as detailed in SI S1), but not for bleaching effects. Initially, the unexposed area shows negligible polarization dependence (black curve). After the first post-exposure at 90°, the PL intensity exhibits a modulation minimum at 90° (red curve). A second post-exposure at 0° reverses this modulation (blue curve). Subsequent exposures at 90° (3rd to 6th) progressively reintroduce and enhance the anisotropy (pink, green, dark blue curves), demonstrating the ability to reorient the excitation anisotropy within the same region. The overall luminescence intensity gradually decreases due to cumulative bleaching. It is also observed that inducing anisotropy in previously unexposed regions is more efficient than rewriting anisotropy in already modified areas. Nevertheless, the modulation amplitude after re-orientation can reach values comparable to the initial exposure. Similar excitation anisotropy behavior was observed in glycine and sucrose crystals, as presented in SI S2.

2.4. Encryption–decryption algorithm

Fig. 5a illustrates the schematic diagram of the encryption-decryption algorithm using our method. Level-1 information is first inscribed and stored in a transparent organic substrate *via* fs laser direct writing under well-defined parameters. The micrometer-scale spatial resolution achieved in this process enables high data density and storage capacity. Subsequently, level-2 information is encoded and concealed by post-exposure to linearly polarized CW laser light at selected polarization angles. Irrelevant polarization angles can also be used to introduce intentional noise. This post-exposure step can be performed either pixel-by-pixel through scanning or in a single step using structured light beams.[49] Rewriting is achievable by applying longer exposures. Once the information is encrypted, the substrate is modified: level-1 information appears as black-white patterns under an optical microscope and exhibits luminescent features under appropriate excitation light. To decrypt level-2 information, the sample is probed with polarized excitation light. Only when the correct combination of polarization states, which serves as the decryption key, is used, the concealed information becomes visible. Conversely, using an incorrect polarization prevents the retrieval of the encrypted data. Fig. 5b displays a proof-of-concept simulation demonstrating the application of this property for image multiplexing or dual-channel encryption. A checkerboard strategy was employed for spatial multiplexing, where adjacent pixels in the overlapping regions are assigned to different writing angles (*e.g.*, 0° and 90°) to prevent crosstalk. The greyscale levels of the encrypted images were simulated using the intensity data from Fig. 3 without normalization, demonstrating a contrast consistent with the actual experimental results. Notably, due to photobleaching effects, the number of readout cycles is inherently limited, which further protects the information against brute-force attacks.

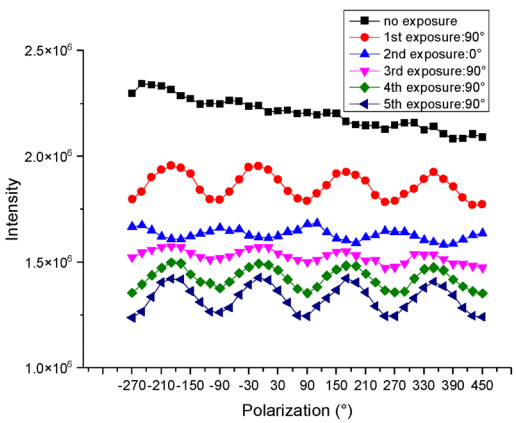

Fig. 4 Photoluminescence intensity at 510 nm as a function of excitation polarization angle for a fixed area (area 3) after successive CW laser post-exposures. The black curve corresponds to the initial state. Red and blue curves represent the responses after the 1st and 2nd post-exposures at 90° and 0°, respectively. Pink, green, and dark blue curves correspond to the 3rd to 6th exposures at 90°. Each exposure duration is 300 s. All curves are corrected for system anisotropy.

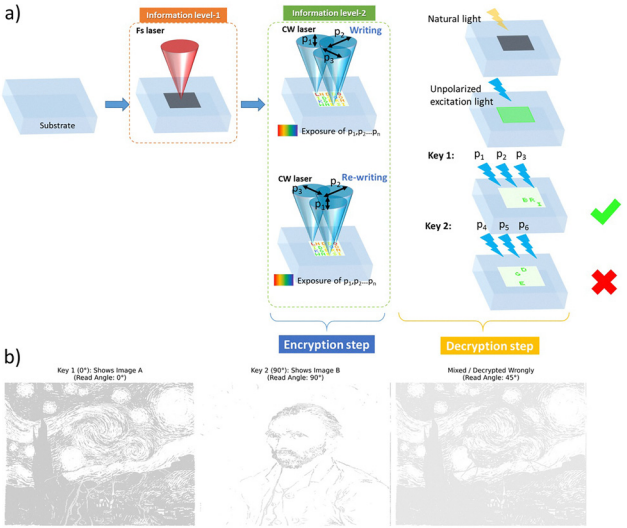

Fig. 5 (a) Schematic diagram of encryption–decryption algorithm. With a proper design, information can only be read out using the appropriate sequence of polarization states (p_1, p_2 and p_3, green check). If probed with incorrect polarization angles (*e.g.*, p_4, p_5 and p_6), false information or noise is retrieved instead (red cross). (b) Simulation of image multiplexing based on the observed properties. The greyscale values are derived directly from the unnormalized intensity data in Fig. 3, reflecting the realistic experimental contrast.

3. Discussion

3.1. The origin of luminescence

During the fs-IR laser direct writing process, high-intensity ultrashort laser pulses induce multiphoton absorption at the focal volume inside the organic material. This results in significant energy absorption by electrons, promoting them into delocalized states and forming a transient electron plasma. The presence of

this plasma rapidly increases the local electronic temperature, which in turn drives non-equilibrium bond breaking and subsequent structural reorganization. Subsequently, as the excited region cools down, new carbon–carbon frameworks form through localized recombination of reactive fragments, ultimately leading to the formation of polycyclic aromatic hydrocarbons or carbon dots (CDs).[41]

3.2. The origin of excitation anisotropy

The luminescence intensity is described through a quasi-chemical reaction scheme involving molecular excitation and relaxation:

$$\mathrm{A} \underset{+h\nu_e,k_e}{\overset{-h\nu_a,k_a}{\rightleftharpoons}} \mathrm{A}^* \tag{1}$$

Here, A and A* denote the molecules in the ground and excited states, respectively. The absorption (k_a) and emission (k_e) rates depend on the electronic structure and photon energies ($h\nu_a$, $h\nu_e$). The intensity of the luminescence is determined by eqn (2) (see details in SI S3):

$$I_{\mathrm{lum}}(h\nu_a, h\nu_e) \propto \frac{k_a(h\nu_a)k_e(h\nu_e)}{k_{-1}}A_0 \sim k_a(h\nu_a)\mathrm{PQY}(h\nu_e)A_0 \tag{2}$$

where $\mathrm{PQY}(h\nu_e) = \dfrac{k_e(h\nu_e)}{k_{-1}}$ is the partial quantum yield, k_{-1} represents the total relaxation rate including both radiative and non-radiative channels. The absorption rate k_a is governed by the interaction between the molecule transition dipole $\boldsymbol{d}$ and the excitation field E_a, described by the dipolar interaction operator: $\hat{D}_a = E_a\boldsymbol{e}_a\cdot\hat{\boldsymbol{d}} = E_a\boldsymbol{e}_a\cdot\hat{\boldsymbol{d}}$, where E_a is the amplitude and $\boldsymbol{e}_a$ is the polarization unit vector of the incoming field. By expressing the field amplitude in terms of the probing light intensity $I_{\mathrm{prob}} = n\varepsilon_0 c E_a^2/2$, the absorption rate is then given by:

$$k_a(h\nu_a) \propto I_{\mathrm{prob}}\cdot\left|\left\langle\psi_{\mathrm{exc}}|\boldsymbol{e}_a\cdot\hat{\boldsymbol{d}}|\psi_g\right\rangle\right|^2\delta\left(E_{\psi_{\mathrm{exc}}} - E_{\psi_g} - h\nu_a\right) \tag{3}$$

Therefore, the dependence on excitation polarization $\boldsymbol{e}_a$ arises from the transition matrix element $\langle\Psi_{\mathrm{exc}}|\boldsymbol{e}_a\cdot\hat{\boldsymbol{d}}|\Psi_g\rangle$, whose value depends on the alignment between the polarization direction and the molecular transition dipole, and is nonzero only when the spatial symmetry of the initial and final states allows the transition.[50]

Considering a luminophore with reference axes X, Y, Z, an anisotropic response arises only if one axis (say, along angle φ) has a non-zero dipole transition moment. In the lab frame (x, y, z), with excitation polarization angle θ, the dipole coupling gives:

$$\langle\Psi_{\mathrm{exc}}(\varphi)|\boldsymbol{e}_a\cdot\hat{\boldsymbol{d}}|\Psi_g\rangle = \mathrm{d}(h\nu_a)\cos(\theta - \varphi) \tag{4}$$

and the absorption rate becomes:

$$k_a(I_{\mathrm{prob}}, h\nu_a, \theta, \varphi) = I_{\mathrm{prob}}\cdot[d_a(h\nu_a)]^2\cos^2(\theta - \varphi) \tag{5}$$

Assuming $\dfrac{\delta A_0}{\delta\varphi}(\varphi)$ the luminophore orientation distribution, the total luminescence intensity is obtained by integration over all directions of luminophore for excitation polarization θ, expressed as:

$$I_{\mathrm{lum}}\left(I_{\mathrm{prob}}, h\nu_a, h\nu_e, \theta\right) \propto I_{\mathrm{prob}}PQY(h\nu_e)\int_0^{2\pi}R(h\nu_a, \theta, \varphi)\frac{\delta A_0}{\delta\varphi}(\varphi)\mathrm{d}\varphi \tag{6}$$

with term $R(h\nu_a,\theta,\varphi) = [d_a(h\nu_a)]^2\cos^2(\theta - \varphi)$ is the response to the light probe of the luminophore direction distribution.

If the luminophore orientation distribution is isotropic, *i.e.*, $\dfrac{\delta A_0}{\delta\varphi}(\varphi) = \text{constant}$, the integral becomes independent on θ, and no excitation anisotropy is observed—as is the case in isotropic media such as liquids or glasses.

In conclusion, anisotropy arises only when both the luminophores are asymmetric and their orientation distribution is anisotropic, as described by Weigert's law.[51] If the luminophore's point group symmetry allows multiple non-zero dipole directions, the angular dependence is more complex, but the overall conclusion remains unchanged.

3.3. Writing and rewriting by polarization dependent bleaching

Bleaching is evident during our emission-spectrum measurements, yet the spectral shape remains unchanged for all excitation-polarization angles (SI S1), indicating that a single luminophore species participates in the process. We suggest that the anisotropy creation and reorientation phenomenon is due to this irreversible polarization direction-sensitive bleaching process, which is related to the destruction of the luminophore by a post-exposure to the excitation light according to linear polarization direction. This can be described for instance as a supplementary reaction that transforms A* into a species B, like in the process presented below:

$$\mathrm{A} \underset{+h\nu_e,k_e}{\overset{-h\nu_a,k_a}{\rightleftharpoons}} \mathrm{A}^* \xrightarrow{k_b,\mathrm{thermal}} \mathrm{B} \tag{7}$$

By solving the boundary conditions of population of species A, A* and B, the luminescence intensity is expressed as follows:

$$I_{\mathrm{lum}}(h\nu_a, h\nu_e, \theta, t) = I_{\mathrm{prob}}\mathrm{PQY}(h\nu_e)\cdot\int_0^{2\pi}R(h\nu_a, \theta, \varphi) \times f\left(t, I_{\mathrm{prob}}, R(h\nu_a, \theta, \varphi)\right)\cdot\frac{\delta A_0}{\delta\varphi}(\varphi)\mathrm{d}\varphi \tag{8}$$

here $f\left(t, I_{\mathrm{prob}}, R(h\nu_a, \theta, \varphi)\right) = \exp\left(-\dfrac{I_{\mathrm{prob}}.R(h\nu_a, \theta, \varphi)k_b}{k_{-1} + k_b}t\right)$ is the bleaching function. Remember that θ is the reading laser polarization direction. On the other hand, at the beginning just after creation of PL, the asymmetric luminophore is randomly distributed in orientation *i.e.*, no excitation anisotropy, so $\dfrac{\delta A_0}{\delta\varphi}(\varphi) = \text{constant}$. Therefore, if the reading time is small enough, the bleaching function is close to one and $I_{\mathrm{lum}}(h\nu_a, h\nu_e, \theta, t)$ is independent of θ.

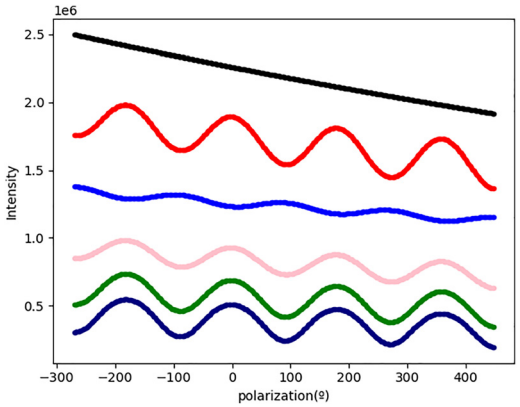

Fig. 6 Simulation results based on eqn (10), corresponding to the experimental conditions in Fig. 4. Full parameter details are provided in SI S4.

However, in the encryption step, when post-exposure polarization is at angle θ_1 and time t_1 long enough, we get the minimum intensity at θ_1. The orientation distribution of the asymmetric luminophore is thus modified by the transformation of the molecules that are aligned along the axis having the largest absorption/excitation amplitude as denoted in the process A to B. It is noted that there is only one species, A, that is bleached for the wavelength we used, as we have detected no spectral distortion in the emission spectrum under bleaching (see SI S1). The exposure changes thus the population of luminophores more along the post-exposure polarization direction. The angular modulation of the PL decreases thus more along this direction and becomes therefore asymmetric. Here the total luminescence can be expressed as below (SI S4):

$$\begin{aligned} &I_{\mathrm{lum}}(h\nu_{\mathrm{a}}, h\nu_{\mathrm{e}}, \theta, \theta_1, t, t_1) \\ &\propto I_{\mathrm{prob}} \int_0^{2\pi} R(h\nu_{\mathrm{a}}, \theta, \varphi) \cdot f\left(t, I_{\mathrm{prob}}, R(h\nu_{\mathrm{a}}, \theta, \varphi)\right) \\ &\cdot f\left(t_1, I_{\mathrm{expo}}, R(h\nu_{\mathrm{a}}, \theta_1, \varphi)\right) \cdot \frac{\delta A_0}{\delta \varphi} \mathrm{d}\varphi \end{aligned} \tag{9}$$

For rewriting step, when a series post-exposures are performed, the distribution is distorted and the response in the same plane shows complex modulations accompanied with a decrease of the overall intensity., as described by eqn (10):

$$\begin{aligned} &I_{\mathrm{lum}}(n, h\nu_{\mathrm{a}}, h\nu_{\mathrm{e}}, \theta, \theta_1, t_i, t) \\ &\propto I_{\mathrm{prob}} \int_0^{2\pi} R(h\nu_{\mathrm{a}}, \theta, \varphi) f\left(t, I_{\mathrm{prob}}, R(h\nu_{\mathrm{a}}, \theta, \varphi)\right) \\ &\times \prod_1^n f\left(t_i, I_{\mathrm{expo}}, R(h\nu_{\mathrm{a}}, \theta_i, \varphi)\right) \frac{\delta A_0}{\delta \varphi} \mathrm{d}\varphi \end{aligned} \tag{10}$$

Fig. 6 shows the simulation results based on eqn (10), modelling the results (Fig. 4) of the fs-laser induced PL in Zeonex glass after a series of post-exposure steps at 0° and 90° used as the writing and rewriting angles θ_i. Details of the parameters used in the simulation are provided in SI S4. The agreement between simulation and experiment supports the proposed bleaching-based mechanism.

4. Conclusions and perspectives

We have demonstrated that fs-laser-induced PL, initially isotropic with respect to excitation polarization, can become anisotropic through post-exposure to linearly polarized light. The anisotropy exhibits a minimum along the post-exposure polarization direction and a maximum perpendicular to it. A longer subsequent exposure allows reorientation of this anisotropy, attributed to polarization-sensitive bleaching of non-spherical luminophores. This writing–rewriting capability has been successfully demonstrated across at least three different types of organic materials.

This technique enables information encoding through controlled anisotropy directions, which is potentially useful for steganography, due to the indirect observability of the excitation anisotropy. Additionally, this method meets several key criteria for effective encryption, including rapid writing, large 3D data storage capacity, stable decryption, erasing capability, broad-spectrum emission, material versatility and compatibility with standard optical systems. To further develop this approach, several key directions are proposed for future study:

4.1. Excitation-wavelength dependence

Investigate whether excitation anisotropy persists under different excitation wavelengths, considering the resonant and wavelength-dependent nature of the absorption process involved in population redistribution.

4.2. Diverse luminophores

Examining other luminophores, including those in Zeonex and beyond, to assess generalizability

4.3. Materials scope

Apply the method to a broader range of organic materials with varied chemical and structural properties.

While this method aligns well with IEDAC goals, further improvement is needed in anisotropy contrast, readout durability, and robustness against photobleaching. Nonetheless, this method provides a versatile platform for secure and rewritable optical data storage.

Author contributions

Conceptualization, R. Q. and B. P.; funding acquisition, B. P. and M. L.; investigation, R. Q., O. P.; methodology, B. P. and R. Q.; project administration, M. L.; resources, O. P., supervision, B. P.; validation, O. P.; visualization, R. Q.; writing original draft, R. Q. and B. P.; writing, review & editing, R. Q., B. P. and O. P. All authors have read and agreed to the published version of the manuscript.

Conflicts of interest

There are no conflicts to declare

Data availability

The data supporting this article have been included as part of the supplementary information (SI). Supplementary information: there are additional information on the raw luminescence signal and its components as long as more results obtained in other materials. There is also a theoretical description of the origin of the luminescence anisotropy and of the bleaching effect. See DOI: https://doi.org/10.1039/d5cp02244d.

The code for luminescent intensity treatment and simulation is available from the authors but it is quite standard.

Acknowledgements

This research was funded by Agence Nationale de la Recherche (ANR), FLAG-IR project, award number ANR-18-CE08-0004-01 project. Ruyue QUE acknowledges the China Scholarship Council (CSC) for the funding of her PhD fellowship, No. 201808440317. We acknowledge the support of Zeon company for providing the sample of Zeonex® 790R.

Notes and references

1 L. Dingand X.-D. Wang, *J. Am. Chem. Soc.*, 2020, **142**, 13558–13564.
2 Z. Ma, J. Zhou, J. Zhang, S. Zeng, H. Zhou, A. T. Smith, W. Wang, L. Sunand Z. Wang, *Mater. Horiz.*, 2019, **6**, 2003–2008.
3 Y. Su, S. Z. F. Phua, Y. Li, X. Zhou, D. Jana, G. Liu, W. Q. Lim, W. K. Ong, C. Yangand Y. Zhao, *Sci. Adv.*, 2018, **4**, eaas9732.
4 H. Sun, S. Liu, W. Lin, K. Y. Zhang, W. Lv, X. Huang, F. Huo, H. Yang, G. Jenkins and Q. Zhao, *et al.*, *Nat. Commun.*, 2014, **5**, 3601.
5 J. Hu, T. Han, Y. Liu, X. Zhang, Y. Duan, Z. Liand and T. Han, *Spectrochim. Acta, Part A*, 2020, **239**, 118486.
6 J. Tang, Z. Li, S. Wan, Z. Wang, C. Wan, C. Daiand Z. Li, *ACS Appl. Mater. Interfaces*, 2021, **13**, 38623–38628.
7 M. Tan, F. Li, X. Wang, R. Fanand G. Chen, *ACS Nano*, 2020, **14**, 6532–6538.
8 W. Ren, G. Lin, C. Clarke, J. Zhouand D. Jin, *Adv. Mater.*, 2020, **32**, 1901430.
9 X. Huang, Q. Guo, S. Kang, T. Ouyang, Q. Chen, X. Liu, Z. Xia, Z. Yang, Q. Zhangand J. Qiu, *ACS Nano*, 2020, **14**, 3150–3158.
10 J. Liu, H. Rijckaert, M. Zeng, K. Haustraete, B. Laforce, L. Vincze, I. Van Driessche, A. M. Kaczmarekand R. Van Deun, *Adv. Funct. Mater.*, 2018, **28**, 1707365.
11 M. Li, W. Yao, J. Liu, Q. Tian, L. Liu, J. Ding, Q. Xue, Q. Luand W. Wu, *J. Mater. Chem. C*, 2017, **5**, 6512–6520.
12 X. Zhan, Z. Zhou, W. Zhou, Y. Yan, J. Yaoand Y. S. Zhao, *Adv. Opt. Mater.*, 2023, **11**, 2200872.
13 M. Song, D. Wang, Z. A. Kudyshev, Y. Xuan, Z. Wang, A. Boltasseva, V. M. Shalaevand A. V. Kildishev, *Laser Photonics Rev.*, 2021, **15**, 2000343.
14 C. Shu, L. Fang, M. Yang, L. Zhong, X. Chenand D. Yu, *Angew. Chem.*, 2022, **134**, e202114182.
15 Z. Lin, H. Wang, M. Yu, X. Guo, C. Zhang, H. Deng, P. Zhang, S. Chen, R. Zengand J. Cui, *J. Mater. Chem. C*, 2019, **7**, 11515–11521; B. Wu, X. Xu, Y. Tang, X. Hanand G. Wang, *Adv. Opt. Mater.*, 2021, **9**, 2101266; B. Wu, N. Guo, X. Xu, Y. Xing, K. Shi, W. Fangand G. Wang, *Adv. Opt. Mater.*, 2020, **8**, 2001192.
16 Y. Fan, X. Jin, M. Wang, Y. Gu, J. Zhou, J. Zhangand Z. Wang, *Chem. Eng. J.*, 2020, **393**, 124799.
17 Z. Liu, L. Zhao, W. Chen, X. Fan, X. Yang, S. Tian, X. Yu, J. Qiuand X. Xu, *J. Mater. Chem. C*, 2018, **6**, 11137–11143.
18 C. Zhu, L. Q. Tao, Z. Peng, G. Wang, Y. Huang, S. Zou, H. Sun, Y. Zhao, X. Chenand T. L. Ren, *Adv. Funct. Mater.*, 2021, **31**, 2103255.
19 L. Liu, R. Zeng, J. Jiang, T. Wu, P. Zhang, C. Zhang, J. Cuiand J. Chen, *Dyes Pigm.*, 2022, **197**, 109919; Z. Long, Y. Wen, J. Zhou, J. Qiu, H. Wu, X. Xu, X. Yu, D. Zhou, J. Yuand Q. Wang, *Adv. Opt. Mater.*, 2019, **7**, 1900006; C. Shi, X. Shen, Y. Zhu, X. Li, Z. Pangand M. Ge, *ACS Appl. Mater. Interfaces*, 2019, **11**, 18548–18554; S. Lin, H. Lin, C. Ma, Y. Cheng, S. Ye, F. Lin, R. Li, J. Xuand Y. Wang, *Light*, 2020, **9**, 22.
20 D. Hu, Y. Lu, Y. Cao, Y. Zhang, Y. Xu, W. Li, F. Gao, B. Cai, B. O. Guan and C. W. Qiu, *et al.*, *ACS Nano*, 2018, **12**, 9233–9239.
21 Q. Zhu, K. Van Vliet, N. Holten-Andersenand A. Miserez, *Adv. Funct. Mater.*, 2019, **29**, 1808191.
22 J. Wu, S. Fu, X. Zhang, C. Wu, A. Wang, C. Li, G. Shanand Y. Liu, *ACS Appl. Mater. Interfaces*, 2020, **12**, 6262–6267.
23 L. Gu, H. Shi, L. Bian, M. Gu, K. Ling, X. Wang, H. Ma, S. Cai, W. Ning and L. Fu, *et al.*, *Nat. Photonics*, 2019, **13**, 406–411.
24 P. She, Y. Ma, Y. Qin, M. Xie, F. Li, S. Liu, W. Huangand Q. Zhao, *Matter*, 2019, **1**, 1644–1655; J. Zhang, S.-X. Tang, R. Fu, X.-D. Xuand S. Feng, *J. Mater. Chem. C*, 2019, **7**, 13786–13793.
25 J. Li, C. Fan, X. Liang, G. Li, X. Xie, R. Zhang, H. Xu, H. Wangand K. Guo, *Chem. Eng. J.*, 2021, **426**, 131293; X. Hou, C. Ke, C. J. Bruns, P. R. McGonigal, R. B. Pettmanand and J. F. Stoddart, *Nat. Commun.*, 2015, **6**, 6884.
26 A. K. Singh, S. Singhand and B. K. Gupta, *ACS Appl. Mater. Interfaces*, 2018, **10**, 44570–44575.
27 H. Wen, B. Wang, H. Zhu, S. Wu, X. Xu, X. Liand and Y. Cao, *Nanomaterials*, 2021, **11**, 1744.
28 G. Shang, Z. Wang, H. Li, K. Zhang, Q. Wu, S. Burokurand and X. Ding, *Photonics*, 2021, **8**, 135; H. Gao, X. Fan, W. Xiongand and M. Hong, *Opto-Electron. Adv.*, 2021, **4**, 210030; A. K. Yetisen, H. Butt, T. Mikulchyk, R. Ahmed, Y. Montelongo, M. Humar, N. Jiang, S. Martin, I. Naydenovaand and S. H. Yun, *Adv. Opt. Mater.*, 2016, **4**, 1589–1600.
29 H. Wang, Z. Qin, H. Zhou, C. Li, H. Bai, X. Li, Y. Li, J. Zhang, S. Quand and L. Huang, *Laser Photonics Rev.*, 2023, **17**, 2200545.
30 Z. Meng, Y. Wu, J. Ren, X. Li, S. Zhangand and S. Wu, *ACS Appl. Mater. Interfaces*, 2022, **14**, 12562–12570.

31 D. Li, Z. Feng, Y. Han, C. Chen, Q. W. Zhangand and Y. Tian, *Adv. Sci.*, 2022, **9**, 2104790.
32 Y. Bao, Y. Yu, H. Xu, Q. Lin, Y. Wang, J. Li, Z.-K. Zhouand and X.-H. Wang, *Adv. Funct. Mater.*, 2018, **28**, 1805306.
33 E. Almeida, O. Bittonand and Y. Prior, *Nat. Commun.*, 2016, **7**, 12533.
34 H. Liu, B. Zhang, T. Gao, X. Wu, F. Cuiand and W. Xu, *Nanoscale*, 2019, **11**, 5506–5511.
35 A. O. Omoniyi, Y. Wang, S. Yang, J. Liu, J. Zhangand and Z. Su, *Mater. Today Commun.*, 2023, **36**, 106508.
36 P. Anderson, E. B. Aranas, Y. Assaf, R. Behrendt, R. Black, M. Caballero, P. Cameron, B. Canakci, T. De Carvalhoand and A. Chatzieleftheriou. Project Silica: towards sustainable cloud archival storage in glass. *In Proceedings of the 29th Symposium on Operating Systems Principles*, 2023; pp. 166–181;; A. Royon, K. Bourhis, M. Bellec, G. Papon, B. Bousquet, Y. Deshayes, T. Cardinaland and L. Canioni, *Advanced Materials*, 2010, **22**, 5282–5286.
37 J. Lu, J. Tian, B. Poumellec, E. Garcia-Caurel, R. Ossikovski, X. Zengand and M. Lancry, *Light: Sci. Appl.*, 2023, **12**, 46.
38 J. Cao, M. Lancry, F. Brisset, L. Mazerolles, R. Saint-Martinand and B. Poumellec, *Cryst. Growth Des.*, 2019, **19**, 2189–2205.
39 J. Zhang, M. Gecevičius, M. Beresnaand and P. G. Kazansky, *Phys. Rev. Lett.*, 2014, **112**, 033901; E. N. Glezer, M. Milosavljevic, L. Huang, R. J. Finlay, T. H. Her, J. P. Callanand and E. Mazur, *Opt. Lett.*, 1996, **21**, 2023–2025; E. Bricchi, B. G. Klappaufand and P. G. Kazansky, *Opt. Lett.*, 2004, **29**, 119–121.
40 J. H. Stricklerand and W. W. Webb, *Opt. Lett.*, 1991, **16**, 1780–1782; D. L. N. Kallepalli, A. M. Alshehri, D. T. Marquez, L. Andrzejewski, J. C. Scaianoand and R. Bhardwaj, *Sci. Rep.*, 2016, **6**, 26163.
41 S. Hayashi, K. Tsunemitsuand and M. Terakawa, *Nano Lett.*, 2022, **22**, 775–782.
42 R. Que, L. Houel-Renault, M. Temagoult, C. Herrero, M. Lancryand and B. Poumellec, *Opt. Mater.*, 2022, **133**, 112651.
43 D. L. N. Kallepalli, A. T. K. Godfrey, J. Walia, F. Variola, A. Staudte, C. Zhang, Z. J. Jakubekand and P. B. Corkum, *Opt. Express*, 2020, **28**, 11267–11279.
44 K. L. N. Deepak, R. Kuladeep, S. Venugopal Raoand and D. Narayana Rao, *Chem. Phys. Lett.*, 2011, **503**, 57–60.
45 R. Liu, D. Zhangand and Z. Li, *Int. J. Extreme Manuf.*, 2025, **7**, 045009.
46 J. Liao, D. Zhangand and Z. Li, *Engineering*, 2025, **49**, 61–80.
47 https://www.zeonex.com/pharmaceuticals.aspx.html.
48 D. L. Kallepalli, A. M. Alshehri, D. T. Marquez, L. Andrzejewski, J. C. Scaianoand and R. Bhardwaj, *Sci. Rep.*, 2016, **6**, 26163.
49 J. Lu, M. Hassan, F. Courvoisier, E. Garcia-Caurel, F. Brisset, R. Ossikovski, X. Zeng, B. Poumellecand and M. Lancry, *APL Photonics*, 2023, **8**, 060801.
50 F. A. Cotton, *Chemical applications of group theory*, John Wiley & Sons, 1991; L. M. Falicov, *Group theory and its physical applications*, University of Chicago press, 1966; M. M. Woolfson, *Acta Crystallogr., Sect. A*, 1969, **25**, 641.
51 F. Weigert, *Z. Phys.*, 1921, **5**, 410–427.

